Temporal Imaging Using Dispersive Gradient-Index Time Lenses

Tianwen Han, Hao Chen, Wenwan Li, Bing Wang, and Peixiang Lu, *Fellow, OSA*

***Abstract*—We study the temporal imaging with a gradient-index (GRIN) time lens in which both dispersion and time-varying quadratic phase modulation are introduced. The lens is built by using cross-phase modulation between a signal and a parabolic pump pulse in the nonlinear optical fiber with group velocity dispersion. A general theoretical analysis of temporal imaging by the GRIN time lens is performed in detail. Compared to thin lens in previous studies, the introduction of dispersion, benefits periodic self-imaging of both time waveform and frequency spectrum for optical pulses. Interestingly, the temporal and spectral profiles of the input can be exchanged with each other periodically in the GRIN time lens. By combining the GRIN time lens with dispersive elements on both sides, the temporal waveforms of incident optical pulses can be stretched and compressed. For an input signal composed of multiple pulses experiencing different dispersions, the temporal depth imaging of the signal is realized by scanning the timing of the pump pulse applied on the lens. The study may find great applications in ultrafast optical signal processing and measurement.**

***Index Terms*—Dispersion, fiber nonlinear optics, optical signal processing, ultrafast optics.**

I. Introduction

THE spatial paraxial diffraction is analogous to temporal narrow-band dispersion in terms of space-time duality [1]. Based on this duality, the spatial thin lens can be extended to the time domain. Thus the time lens was created, which imposes a quadratic phase shift in time. By combining a time lens with dispersive elements on both sides, a temporal imaging system can be established, which enables expanding and compressing time waveforms [2]–[8]. In particular, at the Fourier plane of the time lens, the temporal and spectral profiles of the input pulse can be exchanged with each other. The effect has been studied in time-to-frequency and frequency-to-time conversion systems, where the time-to-frequency conversion factor refers to the ratio of temporal shift of the input to spectral shift of the output [9]–[13]. Time lens has also found great applications in time microscope [14], [15], temporal telescope [16], [17], and Talbot effect [18]–[22]. All the schemes are temporal analogies of spatial imaging for planar objects. Recently, non-flat temporal signals were studied in temporal depth imaging by using time lens arrays [23]. Similar to spatial three-dimensional objects which are longitudinally expanded, the non-flat temporal signal is formed by the superposition of optical pulses experiencing different dispersions. By comparing the different images from the time lens array, one can retrieve the dispersion acquired by each pulse. The temporal depth imaging enables the investigation of the dynamics of ultrafast nonperiodic phenomena where dispersion plays an important role, such as optical rogue waves and the evolution of ultrafast pulses in fiber lasers [15], [23]–[27].

The time lenses are usually implemented in crystals or nonlinear fibers. The previous analytical models that describe the time lenses do not take into consideration the dispersion inside the lens and the time lens is considered as a thin lens. The treatment is valid for long-duration optical pulse, the dispersion introduced by the media plays a minor role during pulse propagation. For an ultrashort pulse propagating in the time lens, the dispersion of media will significantly distort the pulse profile [28], [29]. In this regard, the dispersion inside the time lens cannot be neglected. Thereafter, the gradient-index (GRIN) time lens was proposed with both dispersion and quadratic phase modulation [30], [31]. The lens is analogous to a spatial GRIN lens with quadratic index distribution in the lateral direction [32]–[37]. At the same time, the waves therein experience spatial diffraction. It has been reported that the GRIN time lens can be created using electro-optic (EO) crystal under a low-frequency modulation [30]. The applications of the GRIN time lens have also been proposed [31], including time-frequency mapping, temporal filtering, and temporal imaging. However, the phase shift of an EO phase modulator is limited by the maximum driving voltage applied on the crystal, thus a large dispersion is required [31], [38], [39]. In addition, the time-varying quadratic phase envelope is an approximation of a cosine modulation signal in a small region, greatly limiting the time aperture of the lens and the time duration of input optical pulses.

In this work, we shall perform a systematic investigation on temporal imaging using GRIN time lens, which is realized by introducing both dispersion and cross-phase modulation (XPM) in nonlinear optical fibers [31], [40], [41]. Compared to the EO

Manuscript received October 22, 2019; revised December 11, 2019; accepted January 7, 2020. Date of publication January 10, 2020; date of current version April 15, 2020. This work was supported by the National Natural Science Foundation of China under Grant 11674117 and Grant 11974124. *(Corresponding author: Bing Wang.)*

T. Han, H. Chen, W. Li, and B. Wang are with the School of Physics and Wuhan National Laboratory for Optoelectronics, Huazhong University of Science and Technology, Wuhan, Hubei 430074, China (e-mail: hantianwen@hust.edu.cn; chenhao_hust@hust.edu.cn; liwenwan@hust.edu.cn; wangbing@hust.edu.cn).

P. Lu is with the School of Physics and Wuhan National Laboratory for Optoelectronics, Huazhong University of Science and Technology, Wuhan, Hubei 430074, China, and also with the Laboratory for Optical Information Technology, Wuhan Institute of Technology, Wuhan, Hubei 430205, China (e-mail: lupeixiang@hust.edu.cn).

Color versions of one or more of the figures in this article are available online at https://ieeexplore.ieee.org.

Digital Object Identifier 10.1109/JLT.2020.2965615

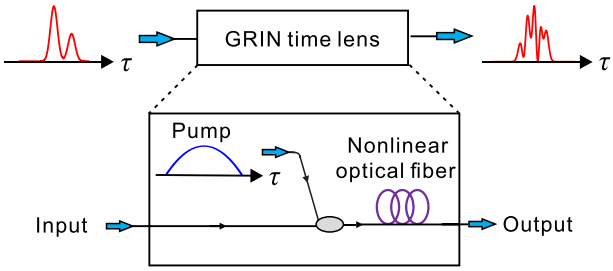

Fig. 1. Schematic of GRIN time lens created by using dispersion and XPM in a nonlinear optical fiber. The pump is a parabolic pulse with high power. τ stands for time variable. The temporal envelope of input signal was distorted after passing through the GRIN time lens.

modulation approach, the XPM method can provide larger phase shift and time aperture by adjusting the power and duration of the pump pulse [22]. We first study the propagation dynamics of an arbitrary optical pulse in the GRIN time lens. The pulse manifests periodic self-imaging in both time and frequency domains. Additionally, the periodical time-to-frequency and frequency-to-time conversion behaviors of the pulse are demonstrated. We also derive the self-imaging period and time-to-frequency conversion factor. A formalism based on temporal *ABCD* matrix is proved to analyze the pulse propagation in the GRIN time lens. Then we create a temporal imaging system based on the GRIN time lens and dispersive elements around. The imaging process is discussed in detail. Finally, a moving GRIN time lens is created to realize temporal depth imaging. The GRIN time lens provides a promising platform for precisely manipulating optical pulses.

II. Propagation Dynamics of Optical Pulses in GRIN Time Lens

The GRIN time lens can be created by using dispersion and XPM in a nonlinear optical fiber, where the latter is induced by a parabolic pump pulse, as shown in Fig. 1. The evolution of the signal in the GRIN time lens can be described by

$$i\frac{\partial A_s(z,\tau)}{\partial z}-\frac{\beta_2}{2}\frac{\partial^2 A_s(z,\tau)}{\partial \tau^2}+2\gamma P_p\left(1-\frac{\tau^2}{\tau_p^2}\right)A_s(z,\tau)=0, \tag{1}$$

where $A_s(z,\tau)$ represents the slowly varying envelope of the signal light with $\tau = t - z/\nu_g$ referring to retarded time in the frame of reference moving at a group velocity ν_g. The real time and propagation distance are denoted by t and z, respectively. β_2 is the group velocity dispersion (GVD) value and γ is the nonlinear coefficient of the fiber. P_p and τ_p are the peak power and half duration of the pump pulse, respectively. The time aperture of the GRIN time lens is given by

$$\tau_a = 2\tau_p. \tag{2}$$

Note that the higher-order effects including third-order dispersion (TOD), self-steepening (SS), and Raman scattering are neglected here. TOD can arouse a significant distortion to the pulse profile as the input pulse width is <1 ps in common optical fibers. SS can lead to an asymmetry in the self-phase modulation-broadened spectra of ultrashort pulses, while the Raman scattering is able to shift the spectrum of an ultrashort pulse toward long wavelengths [42]. It is commonly accepted that the SS and Raman scattering effects can be neglected if the input pulse width is longer than 5 ps [42]. At the same time, the effect of TOD on the pulse propagation is also quite small. Here we consider long-duration input pulses, the influences of TOD, SS and Raman scattering are much weaker than that of GVD and thus can be neglected. In addition, the self-phase modulation (SPM) can give rise to spectral broadening of optical pulses. Nevertheless, due to the weak intensity of signal light compared to the pump light, the effect of SPM is much weaker than that of XPM and can also be ignored. Furthermore, the weak intensity of the signal can also weaken SS and Raman scattering effects.

The eigensolutions of (1) are Hermite-Gaussian functions

$$\varphi_l(\tau)=\left(2^l l!\sqrt{\pi}\right)^{-1/2}H_l\left(\frac{\tau}{\sigma_\tau}\right)\exp\left(-\frac{\tau^2}{2\sigma_\tau^2}\right), \tag{3}$$

where H_l denotes the Hermite polynomial of order l and $\sigma_\tau = (-\beta_2/\alpha)^{1/2}$ with $\alpha = (-4\beta_2\gamma P_p/\tau_p^2)^{1/2}$ is a scale parameter.

For an arbitrary input pulse comprised of superposition of Hermite-Gaussian functions

$$A_s(0,\tau)=\sum_{l=0}^{\infty}a_l\varphi_l(\tau), \tag{4}$$

where a_l is an arbitrary coefficient.

The propagation solution in the GRIN time lens follows

$$A_s(z,\tau)=\exp\left(i2\gamma P_p z-i\frac{\alpha z}{2}\right)\sum_{l=0}^{\infty}a_l\varphi_l(\tau)\exp(-il\alpha z). \tag{5}$$

By performing the Fourier transform of (5), we obtain the corresponding spectrum evolution

$$\tilde{A}_s(z,\omega)=\sqrt{2\pi}\sigma_\tau\exp\left(i2\gamma P_p z-i\frac{\alpha z}{2}\right)\sum_{l=0}^{\infty}(-i)^l a_l\tilde{\varphi}_l(\omega)\exp(-il\alpha z), \tag{6}$$

where

$$\tilde{\varphi}_l(\omega)=\left(2^l l!\sqrt{\pi}\right)^{-1/2}H_l(\sigma_\tau\omega)\exp\left(-\frac{\sigma_\tau^2\omega^2}{2}\right). \tag{7}$$

According to (5) and (6), the initial temporal waveform and spectrum envelope of the pulse are reshaped during propagation due to the different phase accumulation rate for each Hermite-Gaussian component. As the propagation length satisfies the condition $\alpha z = 2m\pi$ with m being a positive integer, all the Hermite-Gaussian components become in-phase. As a result, the pulse propagating in the GRIN time lens exhibits periodic self-imaging in both time and frequency domains. The self-imaging period is given by

$$z_T = 2\pi/\alpha. \tag{8}$$

More interestingly, at the positions of $z = (2m-1)z_T/4$, the pulse undergoes automatic Fourier transforms including time-to-frequency conversion and frequency-to-time conversion. In

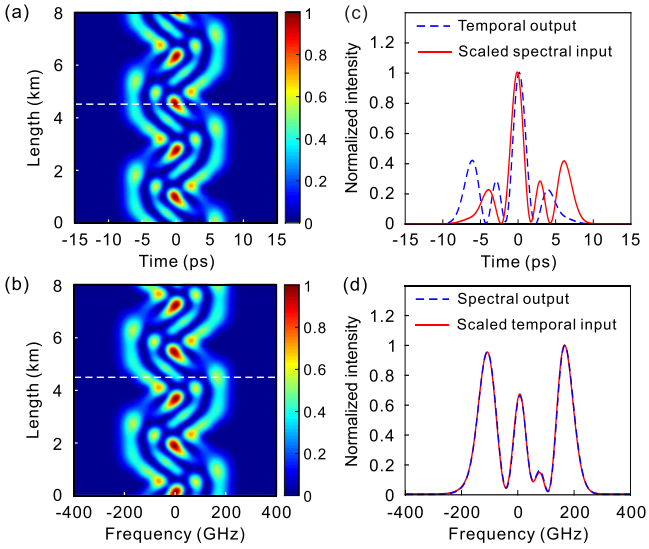

Fig. 2. (a) (b) Temporal and spectral evolutions of the pulse in the GRIN time lens. The white dashed lines denote the position of $z = 4.5$ km. (c) Normalized temporal intensity profile at $z = 4.5$ km and the scaled spectrum envelope at $z = 0$. (d) Normalized spectrum envelope at $z = 4.5$ km and the scaled temporal waveform at $z = 0$.

other words, the temporal profile of the input is converted to the spectral profile of the output, and at the same time the input spectrum envelope is mapped into the output temporal envelope. The relationship between the output temporal waveform and the input spectrum envelope is

$$\left|A_s\left[(2m-1)\frac{z_T}{4},\tau\right]\right|^2 = \frac{1}{2\pi\sigma_\tau^2}\left|\tilde{A}_s\left[0,k\left(\omega=\frac{\tau}{\sigma_\tau^2}\right)\right]\right|^2, \tag{9}$$

where $k = 1$ if m is even and $k = -1$ if m is odd. Likewise, the expression that relates the output spectrum envelope to the input temporal waveform can be written as

$$\left|\tilde{A}_s\left[(2m-1)\frac{z_T}{4},\omega\right]\right|^2 = 2\pi\sigma_\tau^2\left|A_s\left[0,-k\left(\tau=\sigma_\tau^2\omega\right)\right]\right|^2. \tag{10}$$

Thus the time-to-frequency conversion factor is given by

$$\Delta\tau/\Delta\omega = -\beta_2/\alpha, \tag{11}$$

where $\Delta\tau$ is the temporal shift of the input pulse and $\Delta\omega$ denotes the resulting spectral shift.

To confirm the above theoretical analysis, we simulate the evolution of an optical pulse in the GRIN time lens by employing the split-step Fourier method [42]. Here we choose $\beta_2 = -10$ ps^2/km, $\gamma = 20$ W^{-1}km^{-1}, $P_p = 1$ W, and $\tau_p = 16$ ps. The input pulse is formed by the superposition of the first 6-order Hermite-Gaussian functions. According to (8), we calculate the self-imaging period of $z_T = 3.6$ km. The temporal and spectral evolutions of the pulse in the GRIN time lens are shown in Figs. 2(a) and 2(b), where periodic self-imaging phenomena can be clearly seen. The white dotted lines in Figs. 2(a) and 2(b) denote the position of $z = 4.5$ km. The normalized temporal intensity profile at $z = 4.5$ km is a mirror symmetric version of the scaled input spectrum envelope, as presented in Fig. 2(c). Fig. 2(d) depicts the corresponding spectrum envelope at $z =$ 4.5 km, which is a scaled replica of the temporal waveform at $z = 0$. All numerical results agree well with the theoretical predictions of (8)–(11).

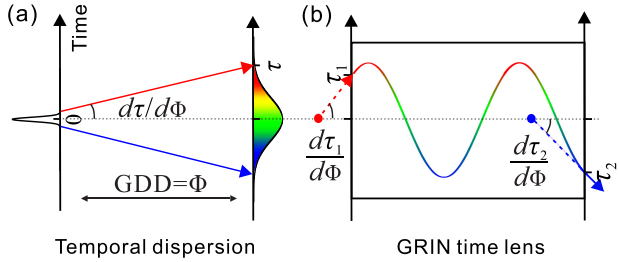

Fig. 3. Temporal ray diagrams of (a) second-order dispersive medium and (b) GRIN time lens. The time ray is characterized by the two vectors of time delay τ and angular frequency $d\tau/d\Phi$. τ_1 and $d\tau_1/d\Phi$ are the time delay and frequency of the time ray on the incident plane of the GRIN time lens, respectively. The time delay and frequency of the time ray on the output plane of the lens are indicated by τ_2 and $d\tau_2/d\Phi$, respectively.

III. *ABCD* Matrices of Second-order Dispersive Medium and GRIN Time Lens

The *ABCD* matrix method in the spatial domain has been widely used to study the effects of optical elements on the paraxial ray, which is described by the radial position r and the gradient dr/dz. By analogy with ray optics the concept of a time ray was introduced, which is described by the two vectors of time delay and frequency sweep [43]–[45]. In addition, the time-domain *ABCD* matrices of optical elements including dispersion, amplitude and frequency modulators, and self-phase modulation were also developed [43], [46]. Here we adopt a different approach to characterize a time ray and derive the *ABCD* matrices of second-order dispersive medium and GRIN time lens.

As shown in Fig. 3(a), a narrow-band pulse will be broadened after passing through a second-order dispersive medium. The medium imposes a quadratic phase modulation on the pulse spectrum. The frequency-domain transfer function of the medium is

$$G_1(\Phi,\omega) = \exp\left(i\frac{\Phi}{2}\omega^2\right), \tag{12}$$

where Φ represents the group delay dispersion (GDD) of the dispersive medium. ω denotes the baseband angular frequency of the pulse. The dispersion will cause redistribution of frequency components of the pulse in time. The relative time delay is given by

$$\delta\tau = \frac{\partial\Delta\varphi(\omega)}{\partial\omega} = \Phi\omega, \tag{13}$$

where $\Delta\varphi(\omega)$ is the spectral phase shift of the pulse induced by the GVD of dispersive medium. In other words, each point on the dispersed pulse corresponds to a different instantaneous frequency, given by $\omega = d\tau/d\Phi$. By exploiting the equivalence between free-space propagation and dispersion, a time ray can be characterized by the two vectors of τ and $d\tau/d\Phi$. The former refers to the position of time ray in the τ axis and its derivative with respect to GDD denotes the frequency of the ray. Note that

there is only the frequency redistribution as a function of time but not new frequency components appear, thus the spectrum of the output pulse is the same with that of the input pulse. Then the *ABCD* matrix of second-order dispersive medium takes the form of

$$M_D = \begin{pmatrix} 1 & \Phi \\ 0 & 1 \end{pmatrix}. \tag{14}$$

For an optical pulse propagating in the GRIN time lens, the relations between incident and output time rays can be written as

$$\tau_2 = A\tau_1 + B\frac{d\tau_1}{d\Phi}, \tag{15}$$

$$\frac{d\tau_2}{d\Phi} = C\tau_1 + D\frac{d\tau_1}{d\Phi}, \tag{16}$$

where τ_1 is the time delay of the incident time ray on the incident plane of the lens. The frequency of the incident time ray is $d\tau_1/d\Phi$. τ_2 and $d\tau_2/d\Phi$ are the time delay and frequency of the output time ray on the output plane of the lens, respectively. *A*, *B*, *C*, and *D* are the four elements of the matrix of GRIN time lens. Based on the analysis in Section II, the time ray propagates in the lens along a periodic oscillation trajectory, as shown in Fig. 3(b). Therefore, all the four matrix elements are periodic functions with respect to z

$$\begin{aligned} A &= a_1\cos(\alpha z) + a_2\sin(\alpha z) \\ B &= b_1\cos(\alpha z) + b_2\sin(\alpha z) \\ C &= c_1\cos(\alpha z) + c_2\sin(\alpha z) \\ D &= d_1\cos(\alpha z) + d_2\sin(\alpha z). \end{aligned} \tag{17}$$

Plugging (17) into (15) and (16), at $z = z_T$, we get $\tau_2 = a_1\tau_1 + b_1\, d\tau_1/d\Phi$ and $d\tau_2/d\Phi = c_1\tau_1 + d_1 d\tau_1/d\Phi$. Based on the self-imaging properties of the pulse in the GRIN time lens, the results of $a_1 = 1$, $b_1 = 0$, $c_1 = 0$, and $d_1 = 1$ can be derived. In addition, at $z = z_T/4$, we have $\tau_2 = a_2\tau_1 + b_2 d\tau_1/d\Phi$ and $d\tau_2/d\Phi = c_2\tau_1 + d_2 d\tau_1/d\Phi$. According to (9)–(11), we deduce $a_2 = 0$, $b_2 = \beta_2/\alpha$, $c_2 = -\alpha/\beta_2$, and $d_2 = 0$. Hence the *ABCD* matrix of GRIN time lens is given by

$$M_G = \begin{pmatrix} \cos(\alpha z) & \frac{\beta_2}{\alpha}\sin(\alpha z) \\ -\frac{\alpha}{\beta_2}\sin(\alpha z) & \cos(\alpha z) \end{pmatrix}. \tag{18}$$

IV. Temporal Magnification and Compression With GRIN Time Lens

By combining the GRIN time lens with dispersive elements on both sides, we can create a temporal imaging system for expanding and compressing time waveforms, as shown in Fig. 4(a). The relationship between the input signal and the output image can be described by

$$\begin{pmatrix} \tau_{\text{out}} \\ \frac{d\tau_{\text{out}}}{d\Phi} \end{pmatrix} = \begin{pmatrix} 1 & \Phi_{\text{out}} \\ 0 & 1 \end{pmatrix} \begin{pmatrix} \cos(\alpha L_G) & \frac{\beta_2}{\alpha}\sin(\alpha L_G) \\ -\frac{\alpha}{\beta_2}\sin(\alpha L_G) & \cos(\alpha L_G) \end{pmatrix} \begin{pmatrix} 1 & \Phi_{\text{in}} \\ 0 & 1 \end{pmatrix} \begin{pmatrix} \tau_{\text{in}} \\ \frac{d\tau_{\text{in}}}{d\Phi} \end{pmatrix}, \tag{19}$$

where Φ_{in} and Φ_{out} are the GDD values of input and output dispersions, respectively. τ_{in} and τ_{out} are the time delays of the input signal and the output image. $d\tau_{\text{in}}/d\Phi$ is the frequency of the incident time ray and $d\tau_{\text{out}}/d\Phi$ is the frequency of the output time ray. For the GRIN time lens with a fixed length L_G, when the input and output dispersions satisfy the imaging condition

$$\left(-\frac{\alpha}{\beta_2}\Phi_{\text{in}}\Phi_{\text{out}} + \frac{\beta_2}{\alpha}\right)\sin(\alpha L_G) + (\Phi_{\text{in}} + \Phi_{\text{out}})\cos(\alpha L_G) = 0, \tag{20}$$

the temporal waveform of the output image is a scaled replica of that of the input signal. The corresponding magnification factor is given by

$$M = \frac{d\tau_{\text{out}}}{d\tau_{\text{in}}} = \cos(\alpha L_G) - \frac{\alpha}{\beta_2}\Phi_{\text{out}}\sin(\alpha L_G). \tag{21}$$

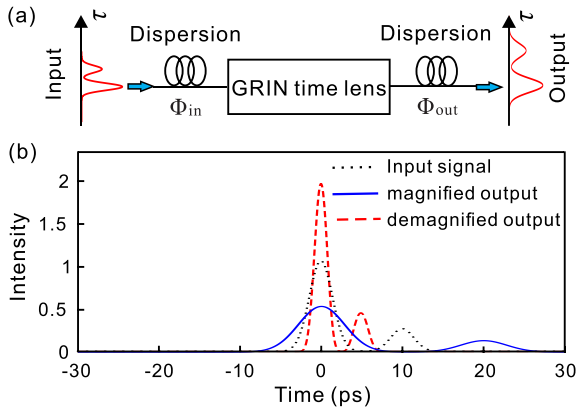

Fig. 4. (a) Schematic diagram of the GRIN time lens-based temporal imaging system. Φ_{in} and Φ_{out} are input and output dispersions, respectively. (b) Temporal waveforms of the input signal and output images. The input signal is depicted by the black dotted curve. The output images corresponding to $M = 2$ and 1/2 are plotted by the blue solid curve and the red dashed curve, respectively.

Fig. 4(b) shows the numerical results in the case of $\alpha L_G = \pi/2$. The input signal consists of two Gaussian pulses with 3.3 ps pulse width and 10 ps separation, as plotted by the black dotted curve in Fig. 4(b). The parameters of the GRIN time lens are chosen as $\beta_2 = -20$ ps^2/km, $\gamma = 20$ W^{-1}km^{-1}, $P_p = 1$ W, and $\tau_p = 40$ ps. For $\Phi_{\text{in}} = 10$ ps^2, the corresponding output dispersion and temporal magnification are $\Phi_{\text{out}} = 40$ ps^2 and $M = 2$, respectively. Thus the input signal is stretched in time and the pulse separation becomes 20 ps, as depicted by the blue solid curve in Fig. 4(b). In addition, the peak power of the output image is half of that of the input signal, satisfying the energy conservation law. On the contrary, as the input and output dispersions are $\Phi_{\text{in}} = 40$ ps^2 and $\Phi_{\text{out}} = 10$ ps^2, respectively, the magnification factor becomes $M = 1/2$. Hence the input signal is compressed in time, as plotted with the red dashed curve in Fig. 4(b). Accordingly, the pulse separation becomes 5 ps and the peak power of the output is twice that of the input.

Next we investigate the influence of the mismatch between input and output dispersions on the temporal imaging. For convenience, we take the GRIN time lens with length $L_G = z_T$ as an example. Then Eq. (19) can be simplified to

$$\begin{pmatrix} \tau_{\text{out}} \\ \frac{d\tau_{\text{out}}}{d\Phi} \end{pmatrix} = \begin{pmatrix} 1 & \Phi_{\text{in}} + \Phi_{\text{out}} \\ 0 & 1 \end{pmatrix} \begin{pmatrix} \tau_{\text{in}} \\ \frac{d\tau_{\text{in}}}{d\Phi} \end{pmatrix}. \tag{22}$$

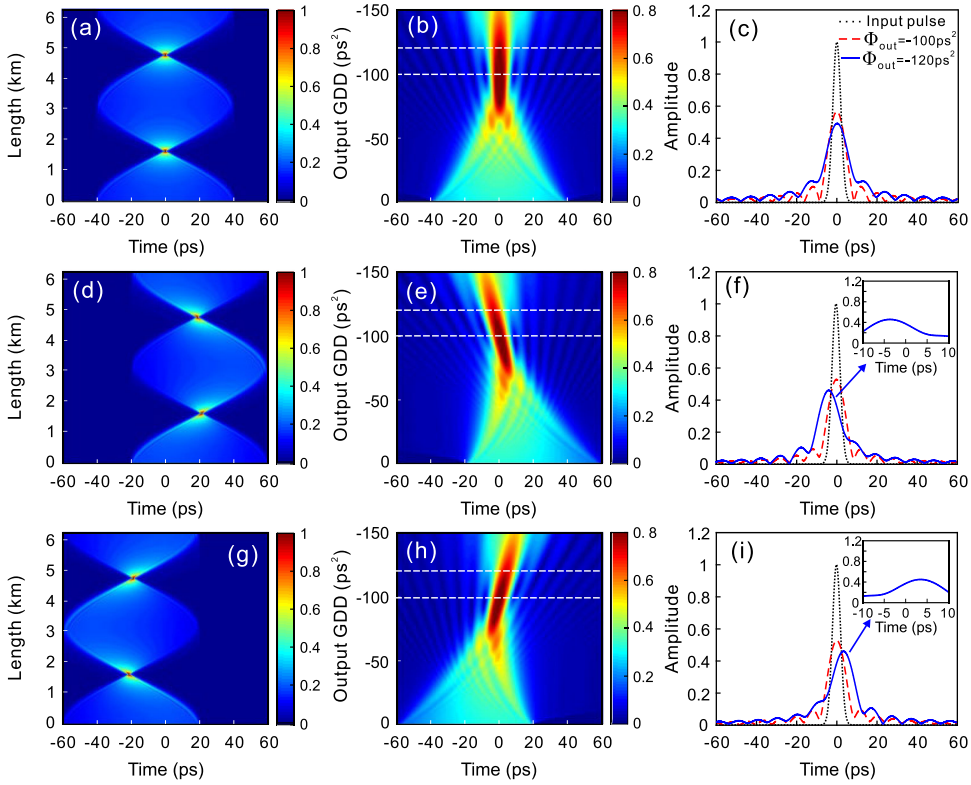

Fig. 5. (a) Temporal evolution of the pulse in the GRIN time lens with timing $\tau_i = 0$. (b) Intensity distribution of the output pulse versus the output dispersion. (c) Temporal waveforms of the input signal and output images. The input signal is depicted by the black dotted curve. The output images at $\Phi_{\rm out} = -100$ ps^2 and -120 ps^2 are plotted by the red dashed curve and the blue solid curve, respectively. (d)−(f) are same to (a)−(c) except for $\tau_i = 20$ ps. (g)−(i) are same to (a)−(c) except for $\tau_i = -20$ ps.

According to (22), the output image has the time delay

$$\tau_{\rm out} = \tau_{\rm in} + (\Phi_{\rm in} + \Phi_{\rm out}) \frac{d\tau_{\rm in}}{d\Phi}. \tag{23}$$

In the case of $\Phi_{\rm out} = -\Phi_{\rm in}$, we have $\tau_{\rm out} = \tau_{\rm in}$ and $M = 1$, indicating that the output image has the same time delay with that of the input signal. In the presence of a mismatch between input and output dispersions, denoted as $\Delta\Phi_{\rm in} = \Phi_{\rm in} + \Phi_{\rm out}$, the image is out of focus and is shifted along the τ axis. The offset is determined by the frequencies of the time rays collected by the GRIN time lens. By moving the GRIN time lens along the τ axis, we can choose different frequency components of the signal to form an image. Here we consider only the central frequency of the time rays entering the GRIN time lens, which is effective for the lens with a small time aperture. Under this condition, (23) is recast into

$$\tau_{\rm out} = \frac{\Phi_{\rm in} - \Delta\Phi_{\rm in}}{\Phi_{\rm in}} \tau_{\rm in} + \frac{\Delta\Phi_{\rm in}}{\Phi_{\rm in}} \tau_i, \tag{24}$$

where τ_i is the timing of the GRIN time lens. By scanning the timing of the pump pulse applied on the lens, we can obtain images with different output time delays.

The theoretical analysis can be verified by implementing numerical simulations. The input signal is a Gaussian pulse with 3.3 ps pulse width and time delay $\tau_{\rm in} = 0$. The input dispersion is $\Phi_{\rm in} = 100$ ps^2. The parameters of the GRIN time lens are the same with that in Fig. 4, corresponding to the time aperture of $\tau_a = 80$ ps. According to (8), the self-imaging period of the pulse in the GRIN time lens is $z_T = 6.3$ km. Fig. 5(a) illustrates the temporal evolution of the pulse in the GRIN time with timing $\tau_i = 0$, where the central frequency of the time rays collected by the lens is $d\tau_{\rm in}/d\Phi = 0$. Hence the center of the pulse after the lens remains $\tau_{\rm out} = 0$ regardless of the magnitude of output dispersion, as shown in Fig. 5(b). When the output dispersion is equal to $\Phi_{\rm out} = -100$ ps^2, a sharp image is observed, as plotted by the red dashed curve in Fig. 5(c). Compared to the input pulse depicted by the black dotted curve, the output one is broadened and distorted, which is induced by the equivalent effect of diffraction of the GRIN time lens with a finite time aperture. The blue solid curve in Fig. 5(c) depicts the image as the output dispersion is $\Phi_{\rm out} = -120$ ps^2. The pulse profile is broadened and distorted more significantly due to both diffraction effect of the GRIN time lens and mismatch between input and output dispersions. Whereas for the GRIN time lens with $\tau_i > 0$, the central frequency of the incident time rays collected by the lens is positive. Fig. 5(d) shows the temporal evolution of the pulse in the GRIN time lens with $\tau_i = 20$ ps. The corresponding intensity distribution of the output pulse versus the output dispersion is presented in Fig. 5(e). As the output negative dispersion increases, the time delay of the output pulse decreases. Similarly, the pulse is focused and forms a sharp image at $\tau_{\rm out} = 0$ when the output dispersion is $\Phi_{\rm out} = -100$ ps^2. Differing from the situation with $\tau_i = 0$, the image is

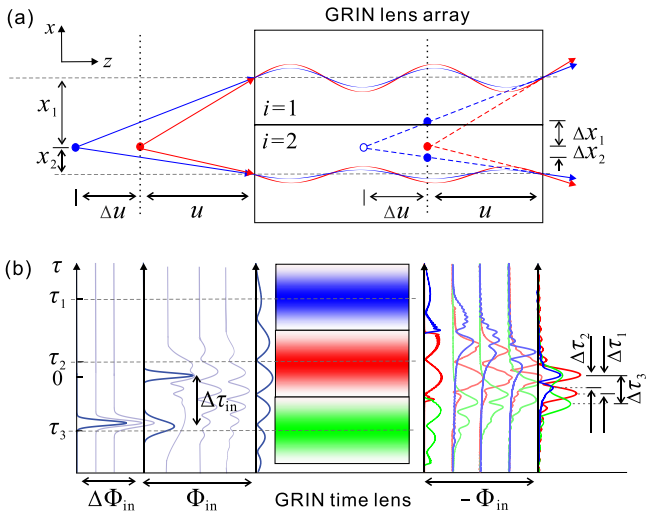

Fig. 6. (a) Schematic of depth imaging system with a GRIN lens array. The distance between the object plane and the incident plane of the lens is u. The corresponding image plane is located at the same distance u behind the output plane of the lens. For an object point shifted by Δu from the object plane, the corresponding image point is also shifted by Δu from the image plane. Since we are measuring at the image plane, the image point is out of focus and is transversally shifted. The offsets Δx_1 and Δx_2 are caused by the lenses with lateral displacements of x_1 and x_2 relative to the object point, respectively. (b) Schematic of temporal depth imaging with a moving GRIN time lens. The input signal is composed of two pulses, which are separated by $\Delta\tau_{\rm in}$. The input dispersions acquired by the two pulses are $\Phi_{\rm in}$ and $\Phi_{\rm in}+\Delta\Phi_{\rm in}$, respectively. The output dispersion is $\Phi_{\rm out}=-\Phi_{\rm in}$. Three images of the signal with pulse separations of $\Delta\tau_1$, $\Delta\tau_2$, and $\Delta\tau_3$ are formed by the GRIN time lens with timings of τ_1, τ_2, and τ_3, respectively.

shifted to $\tau_{\rm out}=-4$ ps in the case of $\Phi_{\rm out}=-120$ ps^2, as the inset in Fig. 5(f) shown, which is in excellent agreement with the theoretical prediction of (24). In addition, the temporal evolution of the pulse in the GRIN time lens with $\tau_i=-20$ ps is illustrated in Fig. 5(g), where the negative frequency components of the pulse are chosen. Fig. 5(h) shows the intensity distribution of the output pulse with respect to the output dispersion, which exhibits an exactly opposite process to that of $\tau_i=20$ ps. As a result, the output image is shifted to $\tau_{\rm out}=4$ ps in the case of $\Phi_{\rm out}=-120$ ps^2, as plotted by the blue solid curve in Fig. 5(i), which is also consistent with the theoretical analysis.

V. Temporal Depth Imaging Based on GRIN Time Lens

In this section, we utilize the GRIN time lens to realize temporal depth imaging. A depth imaging system [47]–[50] in the spatial domain has the ability to distinguish two object points, which are separated along the z axis. Fig. 6(a) shows the schematic of depth imaging with a GRIN lens array. The longitudinal interval between the two object points is denoted by Δu. The object plane is placed at a distance u from the incident plane of the lens. The incident rays with different gradients are collected by the lenses at different positions, corresponding to distinct angular spectrum components of the object. The GRIN lens has a parabolic index profile in the lateral direction, resulting in periodic oscillation trajectories for light rays [32]–[34]. When the GRIN lens length is an integral multiple of the oscillation period of rays, both radial position and gradient of each ray on the output plane are the same as those on the incident plane. Consequently, the point on the object plane forms an image point at the image plane, which is located at the distance u behind the output plane of the lens. The lateral positions of the object point and the image point are also identical. For another object point shifted by Δu from the object plane, the corresponding image point is also shifted to the position at the same distance Δu from the image plane. Since we observe the output at the image plane, the image point is blared and transversally shifted. The offset Δx_i as a function of GRIN lens position is given by

$$\Delta x_i=\frac{\Delta u}{u+\Delta u}x_i, \tag{25}$$

where x_i denotes the lateral displacement of the ith GRIN lens relative to the object point. By measuring Δx_i formed by each GRIN lens in the lens array together with the position of each lens, we can acquire the depth of each point and reconstruct the full depth information of the object.

The temporal counterpart of the depth imaging system based on the GRIN lens is illustrated in Fig. 6(b). A single pulse first propagates along a dispersive medium with GDD $=\Delta\Phi_{\rm in}$ and then another pulse joins. Therefore, the input signal is composed of two pulses experiencing different dispersions. The time interval between the two pulses is $\Delta\tau_{\rm in}$. Next the signal continues to propagate in additional dispersive material with GDD $=\Phi_{\rm in}$ and reaches the incident plane of the GRIN time lens. The GRIN time lens with a finite time aperture imposes temporal and spectral quadratic phase modulations simultaneously on part of the signal, which is determined by the lens timing. Here we choose $L_G=z_T$, thus the signal on the output plane of the lens has the same temporal shape with respect to that on the incident plane. Unlike the spatial imaging system where a virtual image of the object is formed behind the output plane of the GRIN lens, the possibility of having positive or negative dispersion provides an extra degree of freedom in the time domain. The output signal propagates in additional dispersive medium with $\Phi_{\rm out}=-\Phi_{\rm in}$ and reaches the image plane. By moving the GRIN time lens along the τ axis, we can obtain images with different pulse separations. The separation $\Delta\tau_i$ between the two pulses in the image as a function of GRIN time lens timing τ_i is given by

$$\Delta\tau_i=\frac{\Delta\Phi_{\rm in}}{\Phi_{\rm in}+\Delta\Phi_{\rm in}}\tau_i+\frac{\Phi_{\rm in}}{\Phi_{\rm in}+\Delta\Phi_{\rm in}}\Delta\tau_{\rm in}. \tag{26}$$

By measuring pulse separations in the images together with the GRIN time lens timings, we can retrieve the dispersion difference between the two input pulses.

Then we perform numerical simulations to demonstrate the temporal depth imaging with a moving GRIN time lens. In the simulations, the input signal is composed of two Gaussian pulses with 3.3 ps pulse width and separated by $\Delta\tau_{\rm in}=20$ ps. The input dispersions acquired by the two pulses are 100 ps^2 and 120 ps^2, corresponding to $\Phi_{\rm in}=100$ ps^2 and $\Delta\Phi_{\rm in}=20$ ps^2. The output dispersion is $\Phi_{\rm out}=-100$ ps^2. The parameters of the GRIN time lens are the same with those in Fig. 4. The numerical results of the pulse separation in the image for different timings of the GRIN

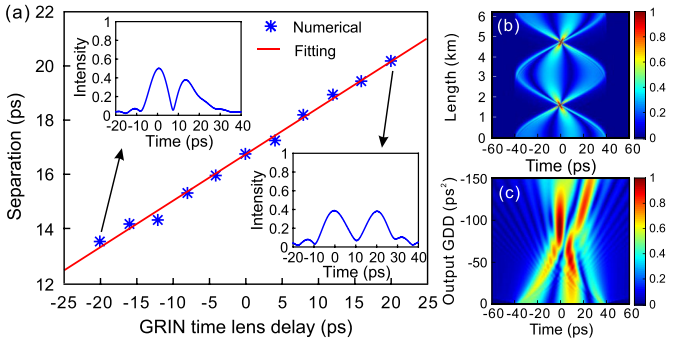

Fig. 7. (a) Numerical results of the pulse separation in the image for different timings of the GRIN time lens. Two insets represent the output images when the GRIN time lens is shifted by −20 ps and +20 ps compared with the input signal, respectively. Red solid line denotes the linear fitted result. (b) Temporal evolution of the signal in the GRIN time lens with timing $\tau_i = 0$. (c) Intensity distribution of the signal after the lens versus the output dispersion.

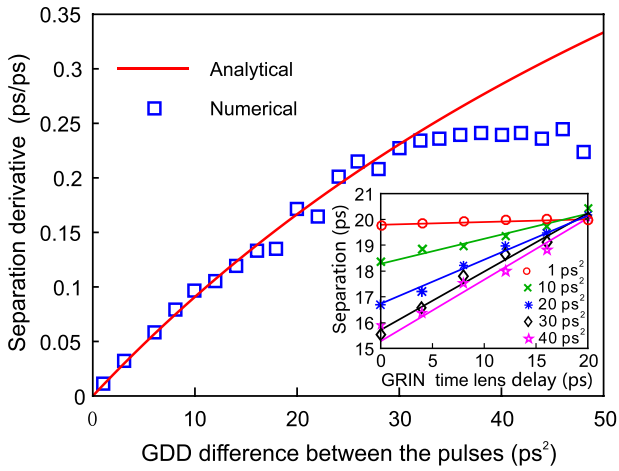

Fig. 8. Numerical (blue squares) and theoretical (red solid curve) results of the separation derivative as a function of the dispersion difference $\Delta\Phi_{\rm in}$. The inset represents five representative numerical results of the pulse separation in the image as a function of GRIN time lens timing for different $\Delta\Phi_{\rm in}$.

time lens are shown in Fig. 7(a). The upper left inset in Fig. 7(a) represents the image when the GRIN time lens is shifted by −20 ps compared with the input signal, showing a pulse separation of $\Delta\tau_i = 13.5$ ps. In contrast, when the GRIN time lens is shifted by +20 ps relative to the input signal, the pulse separation in the image becomes $\Delta\tau_i = 20.2$ ps, as presented in the lower right inset in Fig. 7(a). Fig. 7(b) illustrates the temporal evolution of the signal in the GRIN time lens with timing $\tau_i = 0$. The corresponding intensity distribution of the signal after the lens versus the output dispersion is shown in Fig. 7(c). According to (26), the dispersion difference $\Delta\Phi_{\rm in}$ can be retrieved by taking the derivative of the pulse separation in the image with respect to the GRIN time lens timing. The red solid line in Fig. 7(a) depicts the corresponding linear fitted curve with a slope of

$$\frac{\partial \Delta\tau_i}{\partial \tau_i} = 0.171 \text{ ps/ps}, \tag{27}$$

which indicates that the dispersion difference between the two input pulses is $\Delta\Phi_{\rm in} = 20.63$ ps^2. Compared to the theoretical dispersion difference of $\Delta\Phi_{\rm in} = 20$ ps^2, the numerical error is 3%. The error is resulted from interference between the two pulses in the images.

Next we investigate the sensitivity of our system to changes in the signal dispersion. We observe the pulse separation in the image as a function of GRIN time lens timing for different dispersion difference $\Delta\Phi_{\rm in}$. The inset in Fig. 8 shows five representative numerical results and the corresponding linear fitted curves. The numerical results of the separation derivative as a function of the dispersion difference between the two input pulses are depicted by the blue squares in Fig. 8. We also present theoretical results according to (26), as plotted with the red solid curve in Fig. 8. One can find that the numerical and theoretical separation derivative can agree well with each other when the input dispersion difference is less than 30 ps^2. In particular, if the input dispersion difference is small, such as for $\Delta\Phi_{\rm in} = 1$ ps^2, the defocus effect induced by the mismatch between input and output dispersions is weak. Therefore, the separation derivative is nearly zero, which is close to the situation of $\Delta\Phi_{\rm in} = 0$. On the contrary, for large $\Delta\Phi_{\rm in}$, both diffraction and defocus effects will lead the first pulse to broaden and even overlap with the second pulse at the image plane. Thus two pulses in the images cannot be distinguished clearly and the numerical result deviates the analytical result.

Finally, we discuss the temporal resolution of the proposed system, which refers to the smallest time interval between the two points in the input signal that can be resolved [1]. The temporal resolution degrades due to the finite time aperture of the GRIN time lens. The relationship between output and input fields can be expressed as

$$A(\Phi, \tau) = \int_{-\infty}^{+\infty} h(\tau, \tau_0)\, A(0, \tau_0)\, d\tau_0, \tag{28}$$

where $h(\tau, \tau_0)$ is the response function of the system at τ to an impulse applied at time τ_0 [1]. To find $h(\tau, \tau_0)$, we consider an impulse with time delay τ_0 as the input, given by $A(0, \tau) = \delta(\tau - \tau_0)$, and then the field after the input dispersion becomes

$$A(\Phi_{\rm in}, \tau) = G_1(\Phi_{\rm in}, \tau) * \delta(\tau - \tau_0) = G_1(\Phi_{\rm in}, \tau - \tau_0), \tag{29}$$

where an asterisk denotes convolution. $G_1(\Phi_{\rm in}, \tau)$ is the transfer function of the input dispersion in the time domain, given by

$$G_1(\Phi_{\rm in}, \tau) = \frac{1}{\sqrt{2\pi i \Phi_{\rm in}}} \exp\left(i \frac{\tau^2}{2\Phi_{\rm in}}\right). \tag{30}$$

The GRIN time lens with a time aperture τ_a imposes temporal and spectral quadratic phase modulations on part of the signal simultaneously. As the length L_G of the GRIN time lens is an integral multiple of z_T, the effect of the GRIN time lens on the signal is from only its finite aperture. Then the field on the output plane of the lens can be written as

$$A(\Phi_{\rm in} + \beta_2 L_G, \tau) = G_1(\Phi_{\rm in}, \tau - \tau_0)\, P(\tau), \tag{31}$$

where $P(\tau)$ is the pupil function of the GRIN time lens. For convenience, we assume that the pupil function is rectangular in

time, having the form of

$$P(\tau) = \mathrm{rect}(\tau/\tau_a). \tag{32}$$

Finally, after the output dispersion, we have

$$h(\tau, \tau_0) = G_1(\Phi_{\mathrm{in}}, \tau - \tau_0) P(\tau) * G_2(\Phi_{\mathrm{out}}, \tau), \tag{33}$$

where $G_2(\Phi_{\mathrm{out}}, \tau)$ denotes the transfer function of the output dispersion. According to the convolution integral theorem and the imaging condition $\Phi_{\mathrm{out}} = -\Phi_{\mathrm{in}}$, we obtain

$$h(\tau, \tau_0) = \frac{1}{2\pi|\Phi_{\mathrm{in}}|} \exp\left[i\frac{\pi}{2}\left(\frac{\tau_0^2 - \tau^2}{\Phi_{\mathrm{in}}}\right)\right] \times \int_{-\infty}^{+\infty} P(\tau') \exp\left[2\pi i\left(\frac{\tau - \tau_0}{2\pi\Phi_{\mathrm{in}}}\right)\tau'\right] d\tau'. \tag{34}$$

The integral term in (34) is the Fourier transform of the pupil function. Substituting (32) into (34), we get

$$h(\tau, \tau_0) = \frac{1}{2\pi|\Phi_{\mathrm{in}}|} \exp\left[i\frac{\pi}{2}\left(\frac{\tau_0^2 - \tau^2}{\Phi_{\mathrm{in}}}\right)\right] \mathrm{sinc}\left[\frac{\tau_a(\tau - \tau_0)}{2\pi\Phi_{\mathrm{in}}}\right]. \tag{35}$$

As suggested in Ref. 1, the time from the peak to the first zero of the sinc function can be indicative of the output temporal resolution, corresponding to a time interval of

$$\delta\tau_{\mathrm{out}} = 2\pi|\Phi_{\mathrm{in}}|/\tau_a. \tag{36}$$

According to (22), the temporal magnification of the system is unity, thus the input temporal resolution $\delta\tau_{\mathrm{in}}$ is equal to $\delta\tau_{\mathrm{out}}$. In our simulations, the input dispersion is $\Phi_{\mathrm{in}} = 100\ \mathrm{ps}^2$. If we want to obtain an input resolution $\delta\tau_{\mathrm{in}} = 10$ ps, the time aperture of the GRIN time lens should be greater than 63 ps.

VI. Conclusion

In summary, we have studied the temporal imaging with a GRIN time lens. The lens is built by using dispersion and XPM in a nonlinear optical fiber. The latter is induced by a parabolic pump pulse. Compared to the traditional thin time lens, the introduction of dispersion benefits periodic self-imaging and time-frequency conversion for ultrashort pulses. The self-imaging period and time-to-frequency conversion factor can be manipulated by varying the GVD and nonlinear coefficients of the fiber as well as the power and duration of the pump pulse. By combing the GRIN time lens with dispersive elements on both sides, a temporal imaging system for expanding and compressing time waveforms is created. For an input signal composed of two pulses experiencing different dispersions, the dispersion difference between the two pulses is retrieved by comparing images from different timings of the GRIN time lens. The study provides a promising way to precisely manipulate ultrafast optical pulses and may find wide applications in ultrafast optical signal processing and measurement.

References

[1] B. H. Kolner, "Space-time duality and the theory of temporal imaging," *IEEE J. Quantum. Electron.*, vol. 30, no. 8, pp. 1951–963, Aug. 1994.

[2] B. H. Kolner and M. Nazarathy, "Temporal imaging with a time lens," *Opt. Lett.*, vol. 14, no. 12, pp. 630–632, Jun. 1989.

[3] A. A. Godil, B. A. Auld, and D. M. Bloom, "Picosecond time-lenses," *IEEE J. Quantum Electron.*, vol. 30, no. 3, pp. 827–837, Mar. 1994.

[4] R. Salem, M. A. Foster, A. C. Turner, D. F. Geraghty, M. Lipsom, and A. L. Gaeta, "Optical time lens based on four-wave mixing on a silicon chip," *Opt. Lett.*, vol. 33, no. 10, pp. 1047–1049, May 2008.

[5] B. Li, M. Li, S. Lou, and J. Azaña, "Linear optical pulse compression based on temporal zone plates," *Opt. Exp.*, vol. 21, no. 14, pp. 16814–16830, Jul. 2013.

[6] V. J. Hernandea *et al.*, "104 MHz rate single-shot recording with sub-picosecond resolution using temporal imaging," *Opt. Exp.*, vol. 21, no. 1, pp. 496–203, Jan. 2013.

[7] B. Li and J. Azaña, "Incoherent-light temporal stretching of high-speed intensity waveforms," *Opt. Lett.*, vol. 39, no. 14, pp. 4243–4246, Jul. 2014.

[8] A. Mahjoubfar, D. V. Churkin, S. Barland, N. Broderick, S. K. Turitsyn, and B. Jalali, "Time stretch and its applications," *Nat. Photon.*, vol. 11, pp. 341–351, Jun. 2017.

[9] M. A. Foster, R. Salem, D. F. Geraghty, A. C. Turner-Foster, M. Lipson, and A. L. Gaeta, "Silicon-chip-based ultrafast optical oscilloscope," *Nature*, vol. 456, pp. 81–85, Nov. 2008.

[10] J. Azaña, N. K. Berger, B. Levit, and B. Fischer, "Spectral fraunhofer regime: Time-to-frequency conversion by the action of a single time lens on an optical pulse," *Appl. Opt.*, vol. 43, no. 2, pp. 483–490, Jan. 2004.

[11] P. Guan *et al.*, "Time lens-based optical Fourier transformation for all-optical signal processing of spectrally-efficient data," *J. Lightw. Technol.*, vol. 35, no. 4. pp. 799–806, Feb. 2017.

[12] Z. Qiao *et al.*, "Characterization of ultrashort pulses by time-frequency conversion and temporal magnification based on four-wave mixing at 1μm," *Appl. Opt.*, vol. 56, no. 8, pp. 2294–2300, Mar. 2017.

[13] Y. Duan, L. Chen, H. Zhou, X. Zhou, C. Zhang, and X. Zhang, "Ultrafast electrical spectrum analyzer based on all-optical Fourier transform and temporal magnification," *Opt. Exp.*, vol. 25, no. 7, pp. 7520–7529, Apr. 2017.

[14] C. V. Bennett, R. P. Scott, and B. H. Kolner, "Temporal magnification and reversal of 100Gb/s optical data with an up-conversion time microscope," *Appl. Phys. Lett.*, vol. 65, no. 20, pp. 2513–2515, Aug. 1994.

[15] P. Suret *et al.*, "Single-shot observation of optical rogue waves in integrable turbulence using time microscopy," *Nat. Commun.*, vol. 7, p. 13136, Oct. 2016.

[16] M. A. Foster, R. Salem, Y. Okawachi, A. C. Turner-Foster, M. Lipson, and A. L. Gaeta, "Ultrafast waveform compression using a time-domain telescope," *Nat. Photon.*, vol. 3, pp. 581–585, Sep. 2009.

[17] R. Salem, M. A. Foster, and A. L. Gaeta, "Application of space-time duality to ultrahigh-speed optical signal processing," *Adv. Opt. Photonics*, vol. 5, pp. 274–317, Aug. 2013.

[18] R. Maram, J. V. Howe, M. Li, and J. Azaña, "Noiseless intensity amplification of repetitive signals by coherent addition using the temporal Talbot effect," *Nature Commun.*, vol. 5, p. 5163, Oct. 2014.

[19] L. Lei *et al.*, "Observation of spectral self-imaging by nonlinear parabolic cross-phase modulation," *Opt. Lett.*, vol. 40, no. 22, pp. 5043–5046, Nov. 2015.

[20] T. Han, B. Wang, and P. Lu, "Accelerating self-imaging for airy pulse trains," *Phys. Rev. A*, vol. 99, May 2019, Art. no. 053807.

[21] S. Wang, C. Qin, B. Wang, and P. Lu, "Discrete temporal Talbot effect in synthetic mesh lattices," *Opt. Exp.*, vol. 26, no. 15, pp. 19235–19246, Jul. 2018.

[22] R. Maram and J. Azaña, "Spectral self-imaging of time-periodic coherent frequency combs by parabolic cross-phase modulation," *Opt. Exp.*, vol. 21, no. 23, pp. 28824–28835, Nov. 2013.

[23] A. Klein, T. Yaron, E. Preter, H. Duadi, and M. Fridman, "Temporal depth imaging," *Optica*, vol. 4, no. 5, pp. 502–506, May 2017.

[24] D. R. Solli, C. Ropers, P. Koonath, and B. J alali, "Optical rogue waves," *Nature*, vol. 450, pp. 1054–1058, Dec. 2007.

[25] A. Klein *et al.*, "Ultrafast rogue wave patterns in fiber lasers," *Optica*, vol. 5, no. 7, pp. 774–778, Jul. 2018.

[26] H. Chen, C. Qin, B. Wang, and P. Lu, "Discrete refraction and reflection in temporal lattice heterostructures," *Opt. Lett.*, vol. 44, no. 2, pp. 363–366, Jan. 2019.

[27] Y. Du and X. Shu, "Pulse dynamics in all-normal dispersion ultrafast fiber lasers," *J. Opt. Soc. Am. B*, vol. 34, no. 3, pp. 553–558, Mar. 2017.

[28] F. J. Marinho and L. M. Bernardo, "Electro-optic time lens model for femtosecond pulses," *Proc. SPIE.*, vol. 6994, Apr. 2008, Art. no. 699403.

[29] V. B. Yurchenko, "Improving the accuracy of a time lens," *J. Opt. Soc. Am. B*, vol. 14, no. 11, pp. 2921–2924, Nov. 1997.

[30] F. J. Marinho and L. M. Bernardo, "Graded-index time-lens implementation," *Opt. Lett.*, vol. 31, no. 11, pp. 1723–1725, Jun. 2006.

[31] B. Li and S. Lou, "Time-frequency conversion, temporal filtering, and temporal imaging using graded-index time lens," *Opt. Lett.*, vol. 37, no. 19, pp. 3981–3983, Oct. 2012.
[32] J. Arai, F. Okano, H. Hoshino, and I. Yuyama, "Gradient-index lens-array method based on real-time integral photography for 3-D images," *Appl. Opt.*, vol. 37, no. 11, pp. 2034–2045, Apr. 1998.
[33] F. Okano and J. Arai, "Optical shifter for a 3-D image by use of a gradient-index lens array," *Appl. Opt.*, vol. 41, no. 20, pp. 4140–4147, Jul. 2002.
[34] F. Okano, J. Arai, and M. Okui, "Amplified optical window for 3-D images," *Opt. Lett.*, vol. 31, no. 12, pp. 1842–1844, Jun. 2006.
[35] Y. Zhang, X. Liu, M. R. Belić, W. Zhong, M. S. Petrović, and Y. Zhang, "Automatic Fourier transform and self-Fourier beams due to parabolic potentials," *Ann. Phys.*, vol. 363, pp. 305–315, Dec. 2015.
[36] Y. Zhang, X. Liu, M. R. Belić, W. Zhong, F. Wen, and Y. Zhang, "Anharmonic propagation of 2-D beams carrying orbital angular momentum in a harmonic potential," *Opt. Lett.*, vol. 40, no. 16, pp. 3786–3789, Aug. 2015.
[37] J. Chen, F. Zhang, K. Bian, C. Jiang, W. Hu, and D. Lu, "Dynamics of shape-invariant rotating beams in linear media with harmonic potentials," *Phys. Rev. A*, vol. 99, Mar. 2019, Art. no. 033808.
[38] C. Qin *et al.*, "Spectrum control through discrete frequency diffraction in the presence of photonic gauge potentials," *Phys. Rev. Lett.*, vol. 120, Mar. 2018, Art. no. 133901.
[39] L. Ding *et al.*, "Efficient spectrum reshaping with photonic gauge potentials in resonantly modulated fiber-loop circuits," *Phys. Rev. Appl.*, vol. 12, Aug. 2019, Art. no. 024027.
[40] C. Bersch, G. Onishchukov, and U. Peschel, "Spectral and temporal Bloch oscillations in optical fibers," *Appl. Phys. B*, vol. 104, pp. 495–501, Jul. 2011.
[41] T. Han, H. Chen, C. Qin, W. Li, B. Wang, and P. Lu, "Airy pulse shaping using time-dependent power-law potentials," *Phys. Rev. A*, vol. 97, Jun. 2018, Art. no. 063815.
[42] G. P. Agrawal, *Nonlinear Fiber Optics*. New York, NY, USA: Academic, 2013.
[43] S. P. Dijaili, A. Dienes, and J. S. Smith, "ABCD matrices for dispersive pulse propagation," *IEEE J. Quantum Electron.*, vol. 26, no. 6, pp. 1158–1164, Jun. 1990.
[44] C. V. Bennett and B. H. Kolner, "Aberrations in temporal imaging," *IEEE J. Quantum Electron.*, vol. 37, no. 1, pp. 20–32, Jan. 2001.
[45] B. Li and S. Lou, "Elimination of aberrations due to high-order terms in systems based on linear time lenses," *J. Lightw. Technol.*, vol. 31, no. 13. pp. 2200–2206, Jul. 2013.
[46] M. Nakazawa, H. Kubota, A. Sahara, and K. Tamura, "Time-domain ABCD matrix formalism for laser mode-locking and optical pulse transmission," *IEEE J. Quantum Electron.*, vol. 34, no. 7, pp. 1075–1081, Jul. 1998.
[47] X. Xiao, B. Javidi, M. Martínez-Corral, and A. Stern, "Advances in 3-D integral imaging: Sensing, display, and applications," *Appl. Opt.*, vol. 52, no. 4, pp. 546–560, Jan. 2013.
[48] L. Zhou, X. Zhao, Y. Yang, and X. Yuan, "Voxel model for evaluation of a 3-D display and reconstruction in integral imaging," *Opt. Lett.*, vol. 39, no. 7, pp. 2032–2035, Apr. 2014.
[49] M. Martínez-Corral and B. Javidi, "Fundamentals of 3D imaging and displays: A tutorial on integral imaging, light-field, and plenoptic systems," *Adv. Opt. Photonics*, vol. 10, no. 3, pp. 512–566, Sep. 2018.
[50] H.-L. Zhang, H. Deng, J.-J. Li, M.-Y. He, D.-H. Li, and Q.-H. Wang, "Integral imaging-based 2D/3D convertible display system by using holographic optical element and polymer dispersed liquid crystal," *Opt. Lett.*, vol. 44, no. 2, pp. 387–390, Jan. 2019.

Tianwen Han received the B.S. degree in optical information science and technology from the Taiyuan University of Science and Technology, Taiyuan, China, in 2016. He is currently working toward the Ph.D. degree in physics from the Huazhong University of Science and Technology, Wuhan, China. His research interests include ultrafast optics, fiber nonlinear optics, and frequency comb.

Hao Chen received the B.C. degree in physics from the Huazhong University of Science and Technology, Wuhan, China, in 2016, where he is currently working toward the Ph.D. degree in physics. His research interests include dynamic modulated photonic devices and nonlinear optics.

Wenwan Li received the B.S. degree in new energy science and technology from Fujian normal University, Fuzhou, China, in 2017. She is currently working toward the Ph.D. degree in physics from the Huazhong University of Science and Technology, Wuhan, China. Her research interests include all-optical signal processing and ultrafast optics in optical fiber communications.

Bing Wang received the B.S. degree and the Ph.D. degree in physics from Wuhan University, Wuhan, China, in 2002 and 2007, respectively. He is currently a Professor with the School of Physics and Wuhan National Laboratory for Optoelectronics, Huazhong University of Science and Technology, Wuhan, China. His current research interests include metal/graphene plasmonics, nanophotonics, nonlinear, and ultrafast optics.

Peixiang Lu received the B.S. degree in physics from Peking University, Beijing, China, in 1987, and the Ph.D. degree from the Shanghai Institute of Optics and Fine Mechanics, Chinese Academy of Sciences, Shanghai, China, in 1992. He is currently a Professor with the School of Physics and Wuhan National Laboratory for Optoelectronics, Huazhong University of Science and Technology, Wuhan, China. He is a Fellow of the Optical Society of America. His current research interests include ultrafast optics, laser physics, and nanophotonics.